The electrical and electrochemical properties of graphene nanoplatelets modified $75V_2O_5$–$25P_2O_5$ glass as a promising anode material for lithium ion battery

Mesfin A. Kebede [a,*], Nithyadharseni Palaniyandy[a], Rawya M. Ramadan[b] and Eslam Sheha[c,*]

[a]*Energy Materials, Materials Science and Manufacturing, Council for Scientific and Industrial Research (CSIR), Pretoria 0001, South Africa*

[b]*National Research Center, Dokki, Cairo, Egypt*

[c]*Physics Department, Faculty of Science, Benha University, Benha, Egypt*

Abstract

A V_2O_5 anode material significantly challenged on its further development to be used in lithium ion batteries in-terms of its structural degradation, poor cyclability and low conductivity. Thus researchers started to work on composite matrix such as V_2O_5–P_2O_5 and in this work we synthesized pristine and 7.5% GNP modified $75V_2O_5$–$25P_2O_5$ and used for the first time as anode for lithium-ion batteries; the anodes delivered with corresponding first discharge capacities of ~ 1400 and ~ 1600 mA h g^{-1} (almost equal to theoretical capacity of V_2O_5 1472 mA h g^{-1} during a fully reduction from V^{5+} to V^0), respectively. The rapid capacity fade was observed in the first few initial cycles (up to 10th cycle) for both materials; however highest discharge capacity of 446 mAh g^{-1} was retained after 100th cycles for 7.5% GNP modified $75V_2O_5$–$25P_2O_5$ than unmodified composite, with the capacity retention of 89% with respect to 10th cycle discharge capacity. The electrical conductivity of $75V_2O_5$–$25P_2O_5$ drastically increases with GNP modification. The superior electrochemical performance of $75V_2O_5$–$25P_2O_5$–7.5%GNP attributed to the high electronic and ionic conductivity due to graphene nano-platelets.

*Authors to whom correspondence should be addressed: (**M.A. Kebede and E. Sheha**): E-mail address: mkebede@csir.co.za;ISLAM.SHIHAH@fsc.bu.edu.eg:Tel.:+27128413588;+20133353716;Fax: +27128412135; +20133222578

1. Introduction

Until now and for the years to come, lithium-ion battery (LIB) remains as the effective energy storage system even though other options like magnesium, sodium batteries have become getting research momentum. For LIB to be more competitive it is essential to search for substitutes of the traditional $LiCoO_2$ cathode and graphite anode with high voltage and high capacity electrode materials to improve the energy density of the existing LIBs systems. The anode part of lithium ion battery plays significant role just as the cathode part plays a crucial role. The commercially used conventional graphite-based anode materials for lithium-ion battery not only have low theoretical capacity (372 mA h g^{-1}) but also have low power density which greatly limit their application to match the development of particular high-specific capacity cathode materials[1,2].

Nowadays, alloys (Si-Li, Sn-Li, etc.), metal oxides (MnO, CoO, etc.) and three-dimensional phosphate-based polyanionic structures (VPO_4, $LiVOPO_4$, etc.)[3,4] are getting a great deal of attention as alternative anodes for lithium ion battery applications to the traditional graphite-based anode materials. Unfortunately, anodes using alloys and metal oxides typically known to suffer extensive capacity fading during repeated cycling due to severe volumetric change (for instance ~300% for Si, ~250% for SnO_2, etc.) when they react with lithium electrochemically, which leads to pulverization, cracking and fracturing of the initial particle morphology and thereby structural collapse of active materials[3,5,6]. Interestingly, three-dimensional phosphate based polyanionic structure anodes are more stable unlike alloys and metal oxides based anodes as their larger anions PO_4^{3-} build an open 3D framework for the lithium ion pathway which can help to stabilize the structure by reducing the volume change during the charge and discharge process. Thus, the issue of pulverization is no longer a challenge for phosphate-based polyanionic structures thereby they are so promising anode materials for LIBs.

Recently, amorphous V_2O_5–P_2O_5 has been used as cathode material for magnesium ion batteries and showed improved high-voltage electrochemical magnetization compared to poly-crystalline V_2O_5[7]. Moreover, previously the amorphisation of V_2O_5 through high-temperature melt-quenching with P_2O_5 has been studied as cathodes for Li-ion batteries [8]. Delaizir *et al.* [9] reported that a ternary Li_2O–V_2O_5–P_2O_5 glass system as electrode material for rechargeable lithium batteries and the material shows stabilized cycling behavior over 15 cycles with a relatively small capacity of 75 mA h g^{-1}. The commonly accepted hypothesis about the amorphisation is due to the re-orientation of the V_2O_5 sheets to accommodate the inclusion of PO_4 units. The

theoretical capacity of vanadophosphate (VPO_4) is relatively high about 550 mA h g^{-1}, that can be delivered when 3 lithium ions per molecule intercalate in the electrode material. Since VPO_4 has no good electronic conductivity, the strategy of carbon coating or forming carbon composites improves the electronic conductivity of pristine VPO_4 that in turn enhances the rate performance.

Therefore, in the present manuscript we are reporting for the first time the amorphous GNP modified $75V_2O_5–25P_2O_5$ composite as superior performing anode materials for lithium-ion battery applications. Moreover, this paper explains about the comparison of electrochemical performance of pristine $75V_2O_5–25P_2O_5$ and graphene nanoplatelets modified $75V_2O_5–25P_2O_5$.

2. Experimental

2.1 Material preparation and characterisation

Graphene nanoplatelets Grade M GNP (Electrical conductivity 107 S/m, surface area 120-150 m^2/g) has been imported from XG Science Company. V_2O_5 and P_2O_5 have been sourced from Sisco Research Laboratories Pvt. Ltd. (SRL, India). Analytical grade chemicals GNP, V_2O_5, and P_2O_5 were used as precursors to obtain the vanadophosphate glasses of nominal composition $75V_2O_5–25P_2O_5$ doped with 7.5 wt.% graphene nano-platelets through melting the mixed mixtures in alumina crucibles in an electric furnace at 900 °C for 30 minutes.

The electrode materials crystal structure were characterized using a Rigaku X-ray diffractometer with Fe filtered Cu- Kα ($\lambda = 0.154$ nm) monochromated radiation source. Data were collected in the 2θ range of 10 – 90° at a scan rate of 2°/min. The morphology of the as-synthesized powders was analyzed using a JEOL-JSM 7500F scanning electron microscope (SEM) operated at 2.0 kV. Transmission electron microscope (TEM) and high resolution transmission electron microscope (HR-TEM) images were obtained from a JEOL-Jem 2100 microscope operated at an acceleration voltage of 200 kV. TGA analysis has been recorded with a TA Instruments balance, model TA Q500 instrument. Measurements were carried out on the samples from room temperature (25 °C) to 600 °C under Nitrogen gas flow of 60 mL/min.

2.2 Coin cell fabrication and electrochemical testing

The electrodes for electrochemical testing were prepared by making slurry of 70 wt% active materials of anode samples ($75V_2O_5–25P_2O_5$, and $75V_2O_5–25P_2O_5–7.5\%$ GNP), 15 wt% conducting acetylene black, and 15 wt% polyvinylidene fluoride (PVDF) binder in N-methyl-2-pyrrolidone (NMP) as the solvent. The slurry was coated

on cupper foil using doctor-blade film coater(MTI, USA) followed by vacuum drying at 100 °C for 12 h. The electrodes were cut into circular disk with the diameter of ~16 mm. More details on electrode fabrication reported elsewhere [10-12]. The coin cells were assembled in an argon-filled glove-box (MBraun, Germany) with moisture and oxygen levels maintained at less than 0.1 ppm. Coin cells of 2032 configuration were assembled using lithium foil as reference /counter electrode, Celgard 2400 as separator, 1 M solution of $LiPF_6$ dissolved in 1:1:1 volume ratio mixture of ethylene carbonate (EC), dimethyl carbonate (DMC) and diethylene carbonate (DEC) as the electrolyte. The electrochemical measurements were characterized via a LIR2032 coin-type cells. Cyclic voltammetry (CV) carried out in the voltage window 0.005 to 3.0 V at a can rate 0.1 mV s^{-1} and electrochemical impedance (EIS) analysis were performed using a Bio-Logic VMP3 potentiostat/galvanostat controlled by EC-Lab v10.40 software at a frequency range between 100 kHz and 10 mHz with a perturbation amplitude (rms value) of the ac signal of 10 mV. Every EIS experiment was performed after allowing the electrode to equilibrate for 1 h at the chosen fixed potential. The cells were galvanostatically charged and discharged from 0.005 to 3.0 V at different current densities 200, 500, 1000 and 1500 mA g^{-1} using a Maccor 4000 series battery tester. The specific capacity of the electrode materials in unit mAh g^{-1} refers to the capacity which was calculated using unit mass of the active material of the electrodes alone by excluding the masses of Cu foil, binder and carbon black.

3. Results and discussion

3.1 X-Ray Diffraction and Thermogravimetric analysis

The X-Ray diffraction pattern of pristine $75V_2O_5$–$25P_2O_5$ and graphene nanoplatelets modified $75V_2O_5$–$25P_2O_5$ glassy powders is shown in Fig. 1(a). The X-ray pattern in figure 1(a) did not exhibit the presence of any crystalline plane reflections, demonstrating that the as-synthesised powder electrode materials are structurally amorphous. Graphene nanoplatelets modified V_2O_5–P_2O_5 sample does not show any peak which related carbon, indicating that all the carbons are in the amorphous state.

The thermogravimetric pattern of $75V_2O_5$–$25P_2O_5$ and $75V_2O_5$–$25P_2O_5$–7.5%GNP samples is shown in Fig. 1(b, c). The weight loss from 20 to 200 °C attributed to evaporation of moisture in both $75V_2O_5$–$25P_2O_5$, and $75V_2O_5$–$25P_2O_5$–7.5%GNP samples. Followed by the weight loss from 200–300 °C could be due to condensation of structural hydroxyl groups [13-15] in both materials. The observed weight loss from room temperature to 300 °C is <0.5 % in both materials. Overall, both samples are thermodynamically stable which could enhance the electrochemistry of the batteries.

3.2 SEM and TEM characterization

The SEM micrograph images for $75V_2O_5-25P_2O_5$ and $75V_2O_5-25P_2O_5-7.5\%GNP$ are given in Fig. 2(a, b). The surface of the pristine sample (0 mol% GNP) clearly reveals micro irregular size particles (Fig. 2a), while the morphology drastically changes to large irregular shapes surrounded with a distribution of small particle sizes for $75V_2O_5-25P_2O_5-7.5\%GNP$ (Fig. 2b). Thus the large irregular shapes are the vanadophosphate whereas the small surrounding distributions of particles are the graphene nanoplatelates (GNP). The EDS spectrum in Fig. 2(c, d) show that the intensity of carbon has increased for the GNP modified sample which confirms the presence of GNP.

Fig. 2 (e–h) shows the transmission electron microscopy (TEM), high resolution transmission electron microscopy (HR-TEM), selected area electron diffraction (SAED) (insets) images for the pristine $75V_2O_5-25P_2O_5$ and $75V_2O_5-25P_2O_5-7.5\%GNP$ samples. The HR-TEM images for the samples, did not show lattice fringes due to amorphous nature of the samples (Fig. 2f&h), which is in agreement with the above XRD results and the literature [7]. Instead, a halo pattern was observed for both samples in the SAED which confirmed that the samples are amorphous materials.

3.3 Electrochemical performance analysis

Electrochemical property of $75V_2O_5-25P_2O_5-7.5\%GNP$ and its counterpart pristine $75V_2O_5-25P_2O_5$ electrodes were examined by using cyclic voltammetry (CV) at a scan rate of 0.1 mV s^{-1} in the potential range of 3.0 to 0.005 V. The initial ten cycles cyclic voltammograms of the samples are shown in Fig. 3(a, b). During first cathodic scans the prominent reduction peak appears at 0.55V vs. Li/Li$^+$ for $75V_2O_5-25P_2O_5$ and $75V_2O_5-25P_2O_5-7.5\%GNP$ corresponds to the first lithium insertion and associated to the formation of solid electrolyte interface film due to the decomposition of electrolyte [16]. In the consecutive cycles the cathodic peaks at ~1.05 V and ~0.6 V can be assigned to reductive reaction of VPO_4 glass and the formation of metallic phases V and Li_3PO_4 [7]. While, during anodic process, two successive oxidation peaks found at ~1.25 and ~1.8 V belongs to reversible reaction of metallic phases to VPO_4 glass formation [6]. The $V_2O_5-P_2O_5$ glass system readily can be reduced and leading to VPO_4 [17].

The reversible reaction process can be written as:

$$V + Li_3PO_4 \rightleftarrows VPO_4 + 3Li^+ + 3e^- \qquad\qquad (1)$$

5

There are three lithium ions to react with VPO_4 reversibly, similar to the mechanism proposed in previous reports [18,19]. The cyclic voltammetric (CV) curve show that part of the capacity of the electrode is from non-faradic phenomena. The non-faradic capacity behaviour is typical for conversion oxysalts electrode materials and they are described in literature as conversion materials [20-22]. In the conversion reaction versus lithium the metal ions in the transition metal oxides/oxysalts in the process leads to the reduction of the metal ions to the metallic clusters embedded in a Li_2O matrix that involves the reversible reduction and oxidation of metal oxides, coupled with the formation and decomposition of Li_2O [5,23-25] during lithiation/delithiation. Then the other reduction peaks found at ~2.3 and ~1.6 V for the first cathodic scan of both samples can be related to the continuous phase changes of V_2O_5 to $\gamma\text{-}Li_xV_2O_5$ and $\omega\text{-}Li_xV_2O_5$, respectively after insertion of lithium in to anode matrix [26].

Fig. 4(a) shows the first and second cycle discharge/charge characteristic curves of pristine $75V_2O_5$–$25P_2O_5$ and $75V_2O_5$–$25P_2O_5$–7.5%GNP glassy anode materials cycled between 0.005 and 3.0 V with the current density of 200 mA g^{-1}. During the first discharge-charge, the pristine $75V_2O_5$–$25P_2O_5$ and $75V_2O_5$–$25P_2O_5$–7.5%GNP delivered a specific capacity of 1409-768 and 1644-897 mA h g^{-1} with the corresponding coulombic efficiency of 54.5, 54.6%, respectively. However, their corresponding second cycle discharge capacities are 693 and 812 mA h g^{-1}, respectively. The huge irreversible capacity loss (ICL) were observed in the first cycle can be attributed to the decomposition of the electrolyte and the formation of the SEI films which is in agreement with the CV result [27]. The graphene modified sample has delivered a higher discharge capacity in both the 1st and 2nd cycles. Both the samples show a coulombic efficiency >92% in the 2nd cycle and improving in the next cycles and reaches 99% after 10th cycle which indicates that the as-synthesized samples are a very good reversible for lithium-ion battery application.

In order to get insight into the electrochemical mechanism of lithium storage in $75V_2O_5$–$25P_2O_5$ and $75V_2O_5$–$25P_2O_5$–7.5%GNP electrode, XRD patterns were taken for the samples from the electrode at the charged state (3.0 V) and discharged states (0.8 V), (0.005 V), and are presented in Fig. 4(b, c). Fig. 4(b, c) is the *in-situ* data taken after 1st cycle discharged (DC) states to 0.005 V, 0.8 V and charged (CH) states to 3.0 V of the coin cells. Since, the XRD spectrum dominated by high intensive peaks from the copper substrate we only considered until 40 degrees to exclude the Cu substrate effect. It is clearly observed that the peak at around 18 degree which can be indexed to Li_3PO_4 [19] appears and disappears during discharge as lithium enter the system and discharge/charge as lithium leaves the system for both the samples.

The cyclic performance of $75V_2O_5$–$25P_2O_5$ and $75V_2O_5$–$25P_2O_5$–7.5%GNP glassy system for 100 cycles is shown in Fig. 5(a). At the 100th cycle the $75V_2O_5$–$25P_2O_5$ and $75V_2O_5$–$25P_2O_5$–7.5%GNP samples respectively deliver a capacity of 277 and 447 mA h g^{-1} and with capacity retention of 40% and 55% of their 2nd cycle discharge capacity. It is noteworthy that after the 20th cycle the graphene modified sample shows high stability, 456 mA h g^{-1} (at 20th cycle) and 447 mA h g^{-1} (at 100th cycle) with 98% retention, whereas the pristine 364 mA h g^{-1} (at 20th cycle) and 277 mA h g^{-1} (at 100th cycle) retains only 76%. The graphene nanoplatelets modified sample has shown improved capacity retention and delivered higher capacity.

Fig. 5(b) plots the specific discharge capacity versus cycle number of the electrode materials studied for various current densities of 200, 500, 1000 and 1500 mA g^{-1} with the potential range of 0.005–3.0 V. $75V_2O_5$–$25P_2O_5$–7.5%GNP and its pristine counterpart showed the specific capacity of 752– 633, 359–333, 240–151 and 104–70 mAh g^{-1} corresponding current densities of 200, 500, 1000 and 1500 mA g^{-1}, respectively. The electrodes stability study was done by carrying out deep cycling at 1500 mA g^{-1} and taking back the current density to 200 mA g^{-1}. The specific capacity becomes to around 446–410 mAh g^{-1} in the initial cycles and the capacity reduced to 377–157 mAh g^{-1} at the end of the 100th cycle, at the 100th cycle the GNP modified sample delivered capacity more than double of the pristine. The GNP modified sample showed a superior capacity and stability as compared to pristine $75V_2O_5$–$25P_2O_5$ for all current densities. Specially, for the 200 mA g^{-1} in the case of the rate capacity, $75V_2O_5$–$25P_2O_5$ and $75V_2O_5$–$25P_2O_5$–7.5%GNP respectively retained 38 and 84% of their discharge capacity after 100 cycles. The as-synthesised $75V_2O_5$–$25P_2O_5$–7.5%GNP showed a great potential anode for lithium ion battery as it delivered high capacity and superior electrochemical performance than some related works reported so far and they are summarised in Table 1 [6,16,18].

EIS for electrodes in the coin cells

The lithium ion diffusion kinetics in the as-prepared $75V_2O_5$–$25P_2O_5$ and $75V_2O_5$–$25P_2O_5$–7.5%GNP electrode materials were evaluated by carrying out electrochemical impedance spectroscopy (EIS) using fresh and after 100 cycle coin cells at open circuit voltage (OCV). Figure 6 shows the Nyquist plot for the compound and the impedance spectra were fitted using an equivalent circuit shown in inset of Fig. 6 (b). In the equivalent circuit, R_e corresponds to the combined resistance of electrolyte and cell components. The first semicirle appears at the high frequency region was due to the process of the surface film resistance (R_f) that represents the migration of Li$^+$ ions within the solid electrolyte interface (SEI) film, while at the middle frequency region is due to charge transfer resistance (R_{ct}) which is the Li$^+$ ion charge transfer resistance between the electrodes and electrolyte,

and R_b is the bulk resistance [11]. The CPE(f+dl) is related to the constant phase element arises from the surface film (f) and double layer (dl), and CPE_b is bulk capacitance; C_{int} is for intercalation capacitance. The straight line next to the semicircles represents the Warburg resistance of the composite electrodes, Z_W [28]. The fitting values and fitted elements of the spectra are given in Table 2. The result indicates that for the fresh electrodes, the obtained R_e is 7 and 51 Ω, R_{f+ct} is 293 and 296 Ω for $75V_2O_5$–$25P_2O_5$ and $75V_2O_5$–$25P_2O_5$–7.5% GNP, respectively. After 100 cycle, the resistance (R_{f+ct}) 19 and 16 Ω values of the compounds decreases compared to before cycling which implies that the Li$^+$ ion charge transfer at the interface between the electrode and electrolyte has been improved after cycling. This is evidenced by the stability of the cells becomes higher after repetitive 100 cycles as compared to initial cycles. The fitting errors are lower than 1% and $\chi 2$ is 2.752×10^{-4}.

Electrical properties for the bulk electrode materials

Before we did the coin cell characterisation for two selected samples, we have done thorough investigation for the bulk materials with various GNP concentrations (0%, 2.5%, 5%, 7.5%, and 10%) to choose the best conductive candidate. We have found that 7.5%GNP is the best in terms of electrical conductivity.

The impedance spectra, Z′ versus Z″ for the as-synthesized $75V_2O_5$–$25P_2O_5$ and $75V_2O_5$–$25P_2O_5$–7.5%GNP samples is shown in Fig. 7(a, b). The spectra show depressed semicircle followed by inclined line at low frequencies. The equivalent circuit may be modelled as a parallel combination of a resistance R and a constant phase element for bulk in series with Warburg impedance. The diameter of the semicircles R_b gradually decreases with concentration and temperature rise. The bulk conductivity is calculated using the relation

$$\sigma_b = \frac{t}{R_b A} \tag{2}$$

where A is the surface area of the sample and t is the thickness. Fig. 7(c) shows the GNP concentration dependence of the bulk conductivity at 303 K. The bulk conductivity can be expressed as [29]:

$$\sigma = nq\mu \tag{3}$$

where n is the number of charge carriers and q is the specific charge of the electron $\sim 1.6\text{x}10^{-19}$ C. The increase in the bulk conductivity of V_2O_5–P_2O_5 glassy system with increasing GNP concentration can be related to the increase in the number of mobile charge carriers and free volumes.

The relaxation time can be calculated from the relation [30]:

$$\frac{v}{u} = (\omega\tau)^{1-h} \tag{4}$$

where v denotes the distance on the impedance plot between (O, R_b) and an experimental point, u is the distance between the experimental point and (0, 0) and $h = \frac{2\alpha}{\pi}$

, Fig.7 (a) inset. Fig. 7(d) shows the variation of the relaxation time of $75V_2O_5$–$25P_2O_5$ glassy system as a function of GNP concentrations. The relaxation time decrease from $\sim10^{-5}$ to 10^{-7} sec with increasing GNP content which can be attributed to the change in the free volume of $75V_2O_5$–$25P_2O_5$ glassy system by changing GNP content according to the following equation:

$$\tau(T,\delta) = \tau_0 \exp\left[\frac{b}{(f+\delta)}\right] \tag{5}$$

where δ equal the possible excess free volume V_{ex} to initial equilibrium volume V_∞, $b \sim \gamma V^*/V_\infty$ is a factor close to unity (γ an overlapping factor close to unity, V^* is an activation volume for molecular transport, and $f=V_{eq}/V_\infty$ is the fractional free volume at equilibrium [31].

The frequency dependence of the total conductivity for $75V_2O_5$–$25P_2O_5$ doped by 7.5 mol.% GNP is shown in Fig. 8(a). The glassy system shows two regions of frequency conductivity dispersion, the behaviour can be expressed by the following relation:-

$$\sigma_{ac}(\omega) = \sigma_{dc} + A_1\omega^{S_1} + A_2\omega^{S_2} \tag{6}$$

where A is the frequency independent pre-exponential factor, ω is the angular frequency and s_1, and s_2 are the frequency exponents. The values of the exponents have been obtained using the least square fitting of Eq. (6) for the two regions. Fig.8 (b) shows the temperature dependence of the power exponent for $75V_2O_5$–$25P_2O_5$ doped by 7.5 mol.% GNP. The values of the power exponent in the two regions appear contradictory behaviour.

The s_1 (Region I, (Fig. 8b)) values decreases with temperature indicating that AC conduction mechanism follows the Elliot's correlated barrier hopping model (CBH) [32]. The s_2 (Region II) values increases with temperature indicating that AC conduction mechanism follows small polarons quantum mechanical tunneling model [33]

$$s = 1 - \frac{4}{\ln\left(\frac{1}{\omega\tau_0}\right) - \frac{\omega_H}{K_B T}} \tag{7}$$

9

where σ_{dc} is dc conductivity, ω_H is crossover frequency separating dc regime(plateau region) from the dispersive conduction, k_B is Boltzmann's constant, ω_o is the so called attempt frequency. The transition from CBH conduction mechanism at low frequencies to tunneling conduction mechanism at high frequencies can be attributed to the polaron conduction is predominating at high frequencies.

Fig.8(c) shows the temperature dependence of ac conductivity for $75V_2O_5$–$25P_2O_5$ glassy system doped with different GNP concentrations at 10 kHz. The increase in ac conductivity with increasing temperature show thermally activated process. The σ-1/T are divided into two regions. The activation energy for each region was obtained by fitting the conductivity to Arrhenius equation:-

$$\sigma = \sigma_0 \left(\frac{-E_a}{KT}\right) \qquad (8)$$

where σ_o is a pre-exponential factor and K is the Boltzmann constant. The activation energy values in two temperature regions are listed in Table 3. It is observed that the activation energy E_a in the two regions moderately increase with the increase in concentration of GNP. Although this behaviour contrasts with the results of a relaxation time, but we can accept it, taking into account the dual role of graphene. The first role of graphene is increase in the free volume of the glassy system while, the second role is cut the bridge between the vanadium ions (V^{+4} and V^{+5}). Those two roles were competed each other to produce activation energies by that sight.

4. Conclusions

We synthesized graphene nanoplatelets modified $75V_2O_5$–$25P_2O_5$–7.5%GNP glassy system and evaluated it as anode for LIBs. The $75V_2O_5$–$25P_2O_5$–7.5%GNP glassy anode delivered the first discharge capacity of 1644 mA h g^{-1} and reversible discharge capacity of 812 mA h g^{-1}, much higher than its pristine counterpart $75V_2O_5$–$25P_2O_5$ with first discharge capacity of 1409 mA h g^{-1} and reversible discharge capacity of 693 mA h g^{-1} at 200 mA g^{-1} current density. The GNP modified $75V_2O_5$–$25P_2O_5$ deliver a discharge capacity of 447 mA h g^{-1} at the end of 100 cycles with capacity retention of 55%. It is noted that, after the 20th cycle the graphene modified sample becomes more stable and retains 98% capacity at the end of 100 cycles. The electrical property analysis revealed that, the bulk electrical conductivity drastically increases with GNP modification. This superior electrochemical performance attributed to the high electronic and ionic conductivity due to graphene. This new anode material has potential application to match high voltage cathode materials. In order to improve the capacity and the stability of the anode materials, further work is required to make crystalline VPO_4.

10

Acknowledgment

References

[1] J. Yamaki, H. Takatsuji, T. Kawamura and M. Egashira, Thermal stability of graphite anode with electrolyte in lithium-ion cells, Solid State Ionics 148 (2002) 241-245.

[2] G. Jeong, Y. Kim, H. Kim, Y. Kim and H. Sohn, Prospective materials and applications for Li secondary batteries, Energy & Environmental Science 4 (2011)1986-2002.

[3] H.B. Wu, J.S. Chen, H.H. Hng and X.W.D. Lou, Nanostructured metal oxide-based materials as advanced anodes for lithium-ion batteries, Nanoscale 4 (2012) 2526-2542.

[4] C. Sun, S. Rajasekhara, Y. Dong and J.B. Goodenough, Hydrothermal Synthesis and Electrochemical Properties of $Li_3V_2(PO_4)_3$/C-Based Composites for Lithium-Ion Batteries, ACS applied materials & interfaces 3 (2011) 3772-3776.

[5] M. Kebede, H. Zheng and K.I. Ozoemena, Metal Oxides and Lithium Alloys as Anode Materials for Lithium-Ion Batteries, in *Nanomaterials in Advanced Batteries and Supercapacitors*, ed. nonymous, Springer, (2016), p. 55-91.

[6] J. Zheng, Y. Han, B. Zhang, C. Shen, L. Ming, X. Ou and J. Zhang, Electrochemical Properties of VPO_4/C Nanosheets and Microspheres as Anode Materials for Lithium-Ion Batteries, ACS applied materials & interfaces 6 (2014) 6223-6226.

[7] T.S. Arthur, K. Kato, J. Germain, J. Guo, P. Glans, Y. Liu, D. Holmes, X. Fan and F. Mizuno, Amorphous V_2O_5–P_2O_5 as high-voltage cathodes for magnesium batteries, Chemical Communications 51 (2015) 15657-15660.

[8] Y. Sakurai and J. Yamaki, V_2O_5-P_2O_5 glasses as cathode for lithium secondary battery, J. Electrochem. Society 132 (1985) 512-513.

[9] G. Delaizir, V. Seznec, P. Rozier, C. Surcin, P. Salles and M. Dolle, Electrochemical performances of vitreous materials in the system Li_2O–V_2O_5–P_2O_5 as electrode for lithium batteries, Solid State Ionics 237 (2013) 22-27.

[10] M.A. Kebede, M.J. Phasha, N. Kunjuzwa, M.K. Mathe and K.I. Ozoemena, Solution-combustion synthesized aluminium-doped spinel ($LiAl_xMn_{2-x}O_4$) as a high-performance lithium-ion battery cathode material, Applied Physics A 121 (2015) 51-57.

[11] M.A. Kebede, N. Kunjuzwa, C.J. Jafta, M.K. Mathe and K.I. Ozoemena, Solution-combustion synthesized nickel-substituted spinel cathode materials ($LiNi_xMn_{2-x}O_4$; $0 \leq x \leq 0.2$) for lithium ion battery: enhancing energy storage, capacity retention, and lithium ion transport, Electrochim Acta 128 (2014) 172-177.

[12] N. Kunjuzwa, M.A. Kebede, K.I. Ozoemena and M.K. Mathe, Stable nickel-substituted spinel cathode material ($LiMn_{1.9}Ni_{0.1}O_4$) for lithium-ion batteries obtained by using a low temperature aqueous reduction technique, RSC Advances 6 (2016) 111882-111888.

[13] R. Barde and S. Waghuley, Preparation and electrical conductivity of novel vanadate borate glass system containing graphene oxide, J. Non Cryst. Solids 376 (2013) 117-125.

[14] R. Agrawal, M. Verma, R. Gupta and R. Kumar, Transport property and mixed former effect studies on a new fast Ag+ ion conducting glass system: 0.7[0.75AgI : 0.25AgCl] : 0.3 [Ag_2O: { xB_2O_3: (1-x)MoO_3}], J. Physics D 35 (2002) 810-815.

[15] R. Agrawal, M. Verma, R. Gupta, R. Kumar and R. Chandola, Ion transport and solid state battery studies on a new silver molybdate superionic glass system: x[0.75AgI: 0.25AgCl]: (1-x)[Ag_2O: MoO_3], Ionics 8 (2002) 426-432.

[16] Y. Zhang, X. Zhang, Q. Tang, D. Wu and Z. Zhou, Core–shell VPO_4/C anode materials for Li ion batteries: Computational investigation and sol–gel synthesis, J. Alloys Compounds 522 (2012) 167-171.

[17] C.J. Allen, Advanced cathodes and electrolytes for lithium-ion and lithium-air batteries. (2012).

[18] M. Ren, Z. Zhou and X. Gao, $LiVOPO_4$ as an anode material for lithium ion batteries, J. Applied Electrochemistry 40 (2010) 209-213.

[19] C. Ouyang, S. Shi, Q. Fang and M. Lei, $Li_{1+x}FePO_4$ ($0 \leq x \leq 3$) as anode material for lithium ion batteries: From ab initio studies, J. Power Sources 175 (2008) 891-896.

[20] M.J. Aragón, B. León, C. Pérez Vicente, J.L. Tirado, A.V. Chadwick, A. Berko and S. Beh, Cobalt Oxalate Nanoribbons as Negative-Electrode Material for Lithium-Ion Batteries, Chemistry of Materials 21 (2009) 1834-1840.

[21] M.J. Aragón, B. León, T. Serrano, C.P. Vicente and J.L. Tirado, Synergistic effects of transition metal substitution in conversion electrodes for lithium-ion batteries, Journal of Materials Chemistry 21 (2011) 10102-10107.

[22] M. Chowdhury, O. Oputu, M. Kebede, F. Cummings, O. Cespedes, A. Maelsand and V. Fester, Rapid and large-scale synthesis of Co_3O_4 octahedron particles with very high catalytic activity, good supercapacitance and unique magnetic properties, RSC Advances 5 (2015) 104991-105002.

[23] M. Aragón, C. Pérez-Vicente and J. Tirado, Submicronic particles of manganese carbonate prepared in reverse micelles: A new electrode material for lithium-ion batteries, Electrochemistry Communications 9 (2007) 1744-1748.

[24] M.J. Aragón, B. León, C. Pérez Vicente and J.L. Tirado, Synthesis and Electrochemical Reaction with Lithium of Mesoporous Iron Oxalate Nanoribbons, Inorganic Chemistry 47 (2008) 10366-10371.

[25] X. Nan, C. Liu, K. Wang, W. Ma, C. Zhang, H. Fu, Z. Li, G. Cao, Amorphous VPO_4/C with the enhanced performances as an anode for lithium ion batteries, J. Materiomics 2 (2016) 350-357.

[26] J. Liu, H. Xia, D. Xue, and L. Lu, Double-Shelled Nanocapsules of V_2O_5-Based Composites as High-Performance Anode and Cathode Materials for Li Ion Batteries and V_2O_5-C-SnO_2 Hybrid Nanobelts as High Performance Anodes for Lithium-ion Batteries, J American Chemical Society 131 (2009) 12086–12087.

[27] H. Liu, G. Wang, J. Wang and D. Wexler, Magnetite/carbon core-shell nanorods as anode materials for lithium-ion batteries, Electrochemistry Communications 10 (2008) 1879-1882.

[28] M. Reddy, B.L. Wei Wen, K.P. Loh and B. Chowdari, Energy Storage Studies on $InVO_4$ as High Performance Anode Material for Li-Ion Batteries, ACS applied materials & interfaces **5** (2013) 7777-7785.

[29] G. Prajapati, R. Roshan and P. Gupta, Effect of plasticizer on ionic transport and dielectric properties of PVA–H_3PO_4 proton conducting polymeric electrolytes, Journal of Physics and Chemistry of Solids 71 (2010) 1717-1723.

[30] R. Gamal, E. Sheha, N. Shash and M. El-Shaarawy, Effect of Tetraethylene Glycol Dimethyl Ether on Electrical, Structural and Thermal Properties of PVA-Based Polymer Electrolyte for Magnesium Battery, Acta physica polonica A 127 (2015) 803-810.

[31] A. Alegria, J. Barandiarán and J. Colmenero, Dielectric Relaxation at the Glass Transition as a Free Volume Process. A Single Relaxation Time Approach, Physica status solidi (b) 120 (1983) 349-360.

[32] D. Ramteke and R. Gedam, Study of Li_2O–B_2O_3–Dy_2O_3 glasses by impedance spectroscopy, Solid State Ionics 258 (2014) 82-87.

[33] M. Dult, R. Kundu, J. Hooda, S. Murugavel, R. Punia and N. Kishore, Temperature and frequency dependent conductivity and electric modulus formulation of manganese modified bismuth silicate glasses, J. Non Crystal Solids 423 (2015) 1-8.

Figure captions:

Fig. 1 (a) The XRD pattern of $75V_2O_5$–$25P_2O_5$ and $75V_2O_5$–$25P_2O_5$–7.5%GNP glassy system as-prepared powder samples; The TG pattern for (b) $75V_2O_5$–$25P_2O_5$, and (c) $75V_2O_5$–$25P_2O_5$–7.5%GNP samples.

Fig. 2 (a, b) SEM micrographs, (c, d) EDS spectrum, (e, g) TEM images and (f, h) HR-TEM images including SAED pattern (inset) of the $75V_2O_5$–$25P_2O_5$ and $75V_2O_5$–$25P_2O_5$–7.5%GNP glassy system as-prepared powder samples.

Fig. 3 The initial 10 cyclic voltammetry recorded for (a) $75V_2O_5$–$25P_2O_5$ and (b) $75V_2O_5$–$25P_2O_5$–7.5%GNP glassy system at a scan rate of 0.1 mV s^{-1} in the potential range of 0.005–3.0 V.

Fig. 4 (a) The 1st two cycle charge/discharge voltage profile of a $75V_2O_5$–$25P_2O_5$ and $75V_2O_5$–$25P_2O_5$–7.5%GNP glassy systems at a current density of 200 mA g^{-1}; The XRD pattern of (b) $75V_2O_5$–$25P_2O_5$ and (c) $75V_2O_5$–$25P_2O_5$–7.5%GNP glassy system during the first cycle at the discharged state (0.005 V), (0.8 V) and (3.0 V), respectively.

Fig. 5 (a) The cyclic performance of $75V_2O_5$–$25P_2O_5$ and $75V_2O_5$–$25P_2O_5$–7.5%GNP glassy systems; (b) The rate capability of $75V_2O_5$–$25P_2O_5$ and $75V_2O_5$–$25P_2O_5$–7.5%GNP glassy system.

Fig. 6 The EIS spectrum for coin cells with $75V_2O_5$–$25P_2O_5$ glassy and $75V_2O_5$–$25P_2O_5$–7.5%GNP glassy system (a) fresh and (b) after 100 cycle (inset equivalent circuit).

Fig. 7 (a) Nyquist plot of $75V_2O_5$–$25P_2O_5$ and $75V_2O_5$–$25P_2O_5$ –7.5%NGP (b) $75V_2O_5$–$25P_2O_5$–7.5% GNP glassy system for various temperature, (c) Conductivity, and (d) Relaxation time at 303 K.

Fig. 8 (a) ln(σ) versus ln(F) plots for $75V_2O_5$–$25P_2O_5$ – 7.5% GNP glassy system (b) Power exponent as a function of temperature (c) Temperature dependence of conductivity for different GNP concentrations
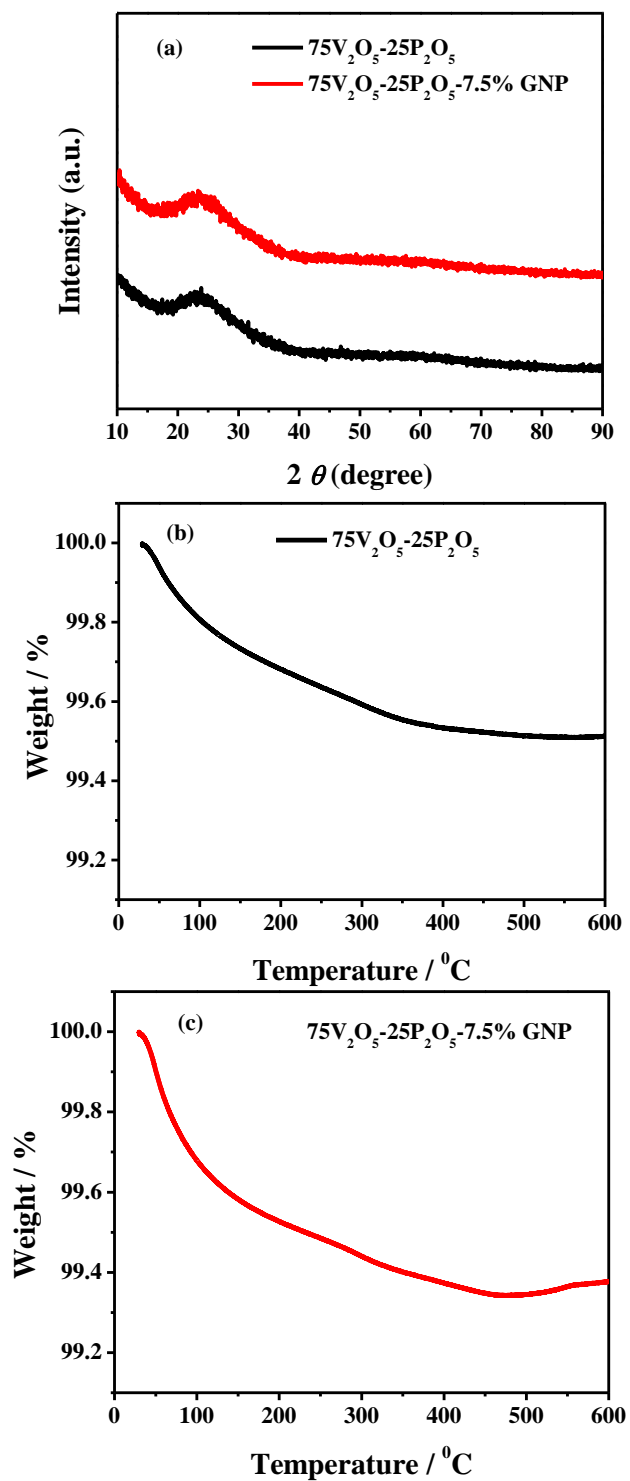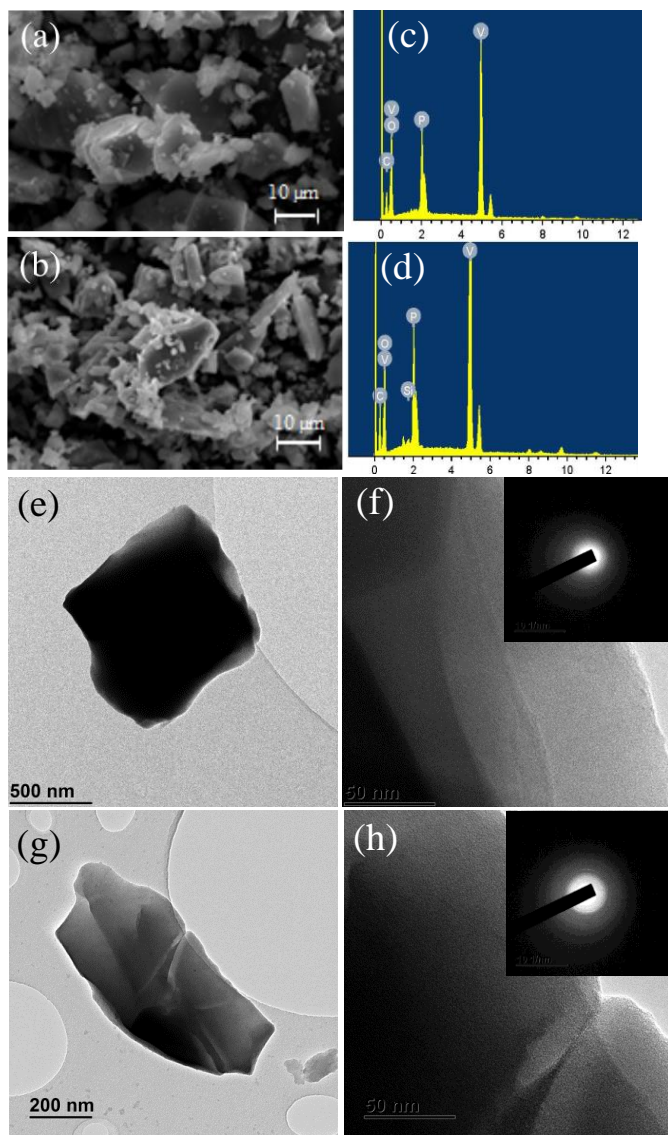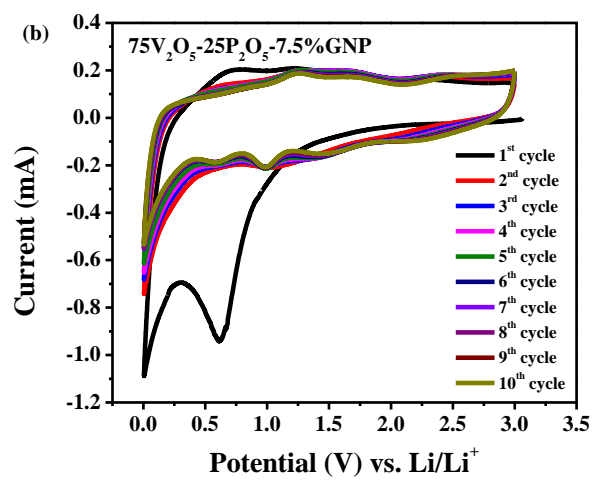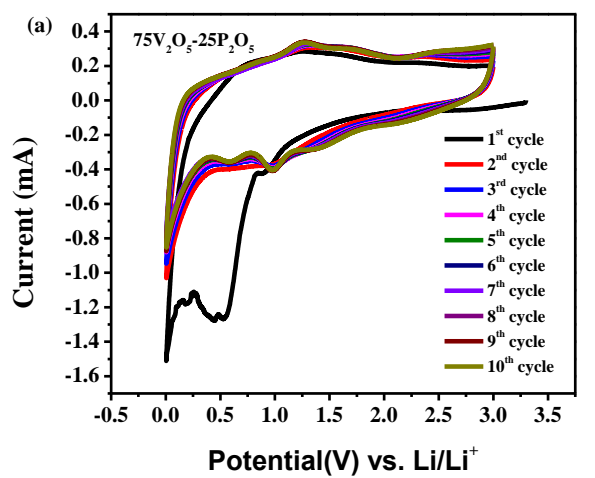
Fig. 1

Fig. 2

Fig. 3

(a) 75V$_2$O$_5$-25P$_2$O$_5$

Legend:
- 1st cycle
- 2nd cycle
- 3rd cycle
- 4th cycle
- 5th cycle
- 6th cycle
- 7th cycle
- 8th cycle
- 9th cycle
- 10th cycle

Y-axis: Current (mA)
X-axis: Potential(V) vs. Li/Li$^+$

(b) 75V$_2$O$_5$-25P$_2$O$_5$-7.5%GNP

Legend:
- 1st cycle
- 2nd cycle
- 3rd cycle
- 4th cycle
- 5th cycle
- 6th cycle
- 7th cycle
- 8th cycle
- 9th cycle
- 10th cycle

Y-axis: Current (mA)
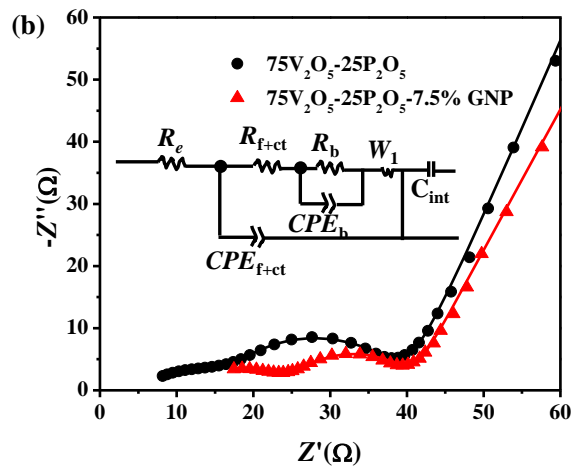X-axis: Potential (V) vs. Li/Li$^+$

Fig. 4
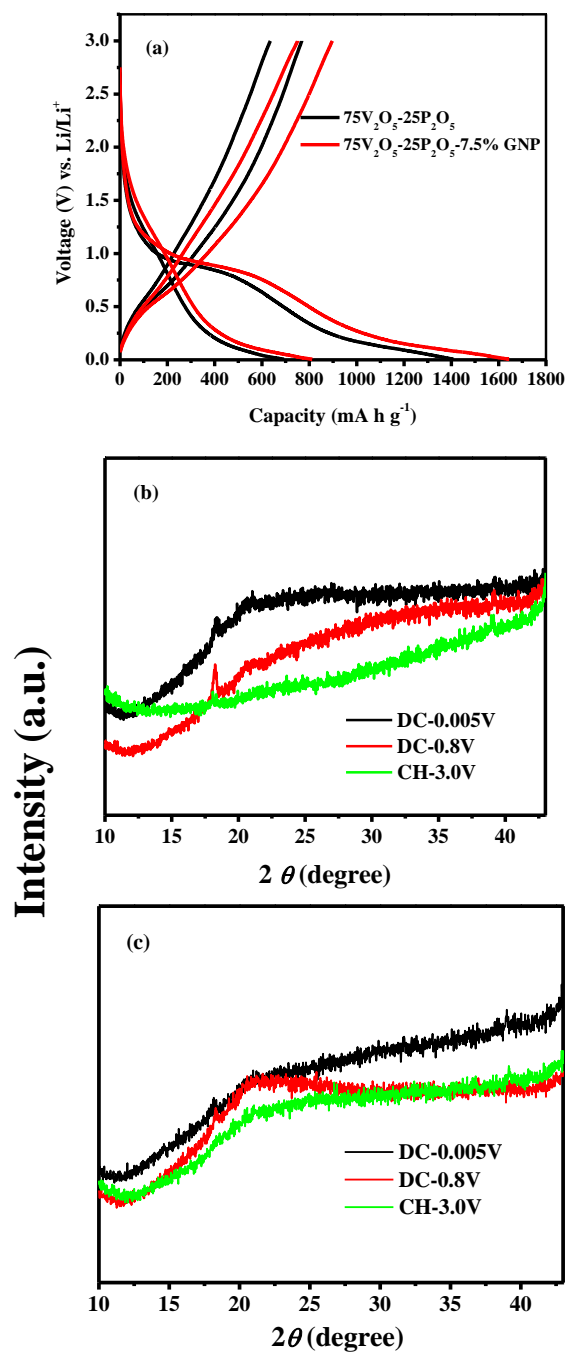
Fig. 5
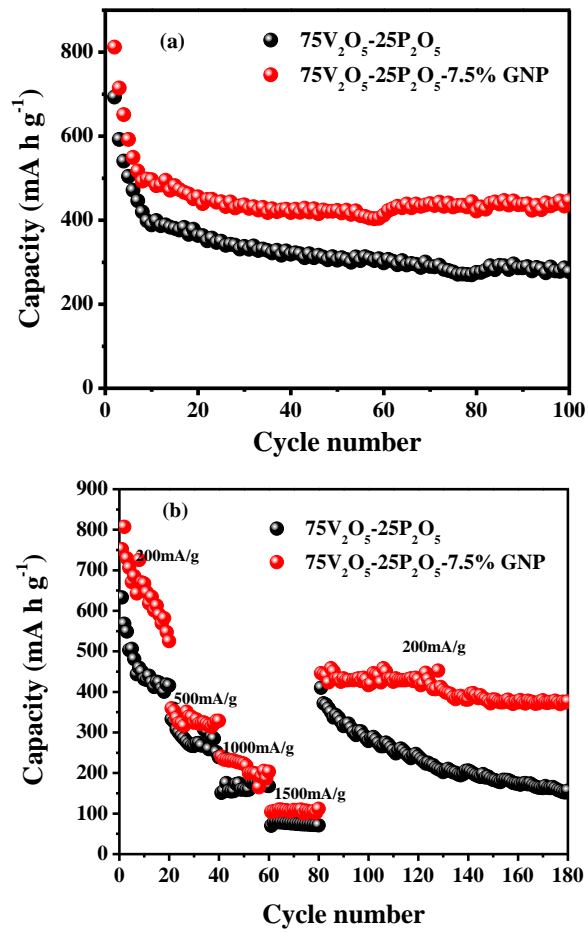
Fig. 6
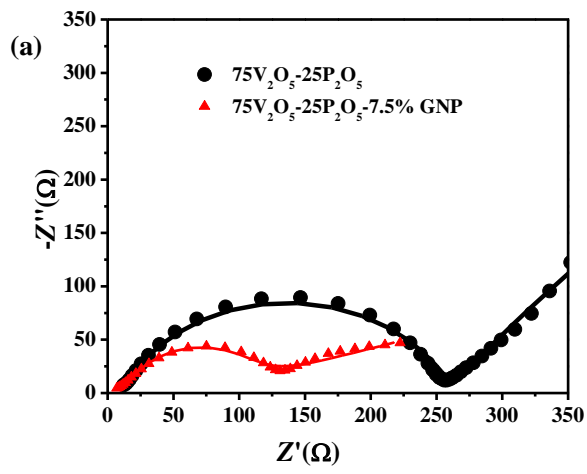
Fig. 7
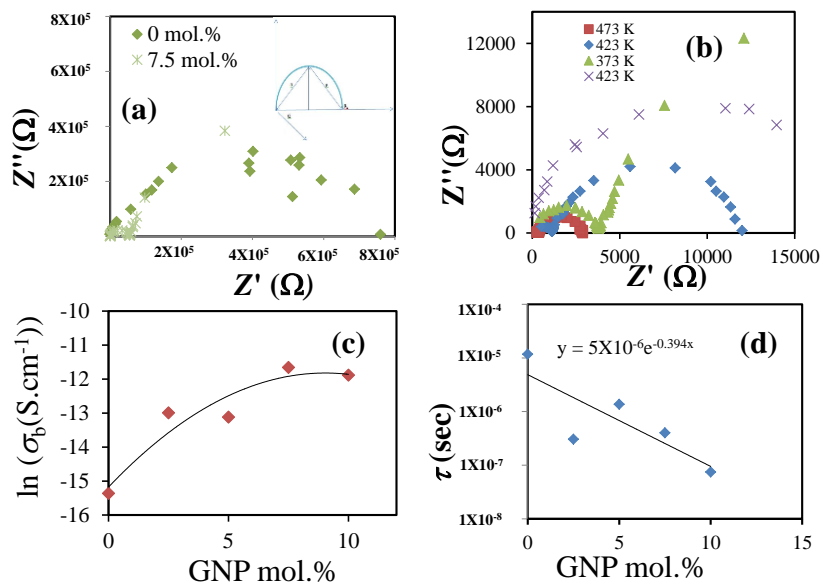
Fig. 8
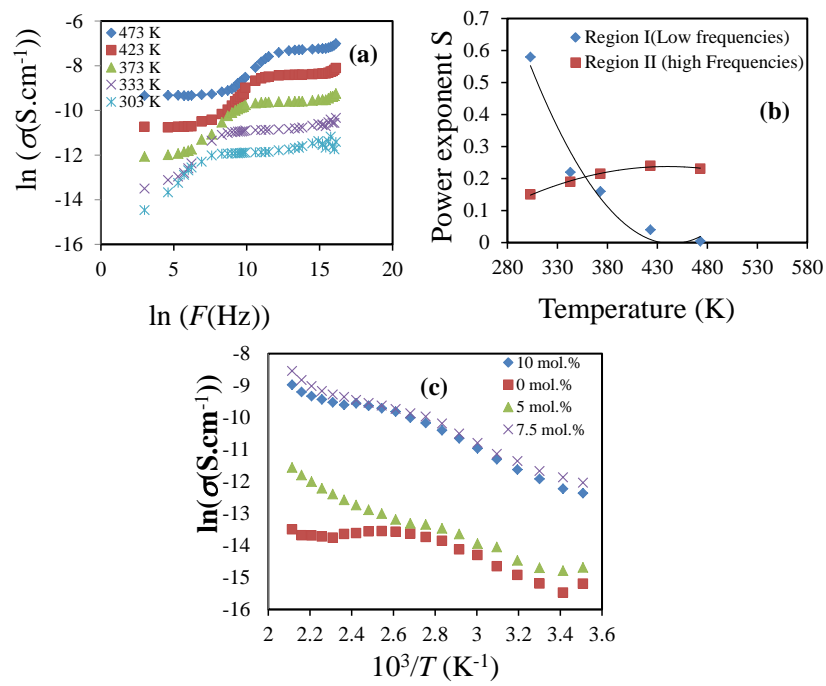
Table 1: The comparison result of this work with previously reported works.

Sample	1st cycle discharge capacity (mAh g^{-1})	2nd cycle discharge capacity (mAh g^{-1})	30th cycle discharge capacity (mAh g^{-1})
VPO$_4$/C	788.7	506.5	230.1
VPO$_4$/C	887.3	502.0	343.0
LiVOPO$_4$	725.5	497.0	380
75V$_2$O$_5$–25P$_2$O$_5$–7.5%GNP	1644.3	897(811.9)	436

Table 2: Fitting results of Nyquist plots of as-synthesized 75V$_2$O$_5$–25P$_2$O$_5$ and 75V$_2$O$_5$–25P$_2$O$_5$–7.5%GNP anode materials.

Sample	$R_e(\Omega)$	R_{f+ct} (Ω)	CPE_{f+dl} (µF)	CPE_b (mF)	R_b (Ω)
Before 100 cycles					
75V$_2$O$_5$-25P$_2$O$_5$	7	293	9055		
75V$_2$O$_5$-25P$_2$O$_5$-7.5%GNP	51	296	12760		
After 100 cycles					
75V$_2$O$_5$-25P$_2$O$_5$	6	19	194	53	11
75V$_2$O$_5$-25P$_2$O$_5$-7.5%GNP	14	16	470	2	8

Table 3: Activation energies of $75V_2O_5–25P_2O_5$ glassy system doped by different GNP concentrations.

GNP mol.%	Ea (273-373 K)	Ea (373-473 K)
0	0.200853	-0.01427
2.5	0.2076	0.023355
5	0.167897	0.17992
7.5	0.2422	0.185975
10	0.26296	0.2076